

Hydrogen Evolution

Vacancy and Dopant Co-Constructed Active Microregion in Ru–MoO_{3–x}/Mo₂AlB₂ for Enhanced Acidic Hydrogen Evolution

Yuquan Yang⁺, Dawei Pang⁺, Chenjing Wang⁺, Zhongheng Fu, Naiyan Liu, Jiajia Liu, Hongjing Wu, Binbin Jia,^{*} Zhonglu Guo,^{*} Xiaoyu Fan,^{*} and Jinlong Zheng^{*}

Abstract: Accurate identification of catalytic active regions is crucial for the rational design and construction of hydrogen evolution catalysts as well as the targeted regulation of their catalytic performance. Herein, the low crystalline-crystalline hybrid MoO_{3–x}/Mo₂AlB₂ with unsaturated coordination and rich defects is taken as the precursor. Through the Joule heating reaction, the Ru-doped MoO_{3–x}/Mo₂AlB₂ catalyst is successfully constructed. Building on the traditional view that individual atoms or vacancies act as active sites, this article innovatively proposes the theory that vacancies and doped atoms synergistically construct active microregions, and multiple electron-rich O atoms within the active microregions jointly serve as hydrogen evolution active sites. Based on X-ray absorption fine structure analysis and first-principles calculations, there is a strong electron transfer among Ru atoms, Mo atoms, and O atoms, leading to extensive O atoms with optimized electronic structure in the active microregions. These O atoms exhibit an H^{*} adsorption free energy close to zero, thereby enhancing the catalytic activity for hydrogen evolution. This work provides a brand-new strategy for the design and preparation of electrocatalytic materials and the systematic regulation of the local electronic structure of catalysts.

Introduction

Hydrogen energy is a green and pollution-free sustainable source of energy. Particularly, green hydrogen produced by electrolyzing water has broad development prospects in replacing traditional fossil energy in the future.^[1–5] In the process of water electrolysis, Pt-based atomic catalysts with high atomic utilization have been proven to exhibit excellent catalytic performance in acidic hydrogen evolution reaction (HER).^[6,7] Among them, Ru, as a platinum group metal, has attracted extensive attention from researchers due to its advantages, such as low cost (one-third of the price of Pt) and similar hydrogen binding strength to Pt.^[8] The electronic state of Ru atomic catalysts is largely related to the local coordination environment between metal atoms and the support. Therefore, designing a novel carrier for Ru atomic catalysts to adjust the overall electronic structure of the

catalyst is the key to optimizing catalytic activity. At present, the metal-support interaction (MSI) of catalysts when using low crystalline materials as carriers is different from that when using crystalline materials as carriers. The abundant defects in the low crystalline substrate can effectively anchor Ru atoms and effectively improve the stability of Ru atomic catalysts during long-term use.^[9,10] However, compared with crystalline materials, low-crystalline materials exposed to highly corrosive or strongly oxidizing environments are usually not durable.^[10,11] Therefore, it is crucial to construct Ru atoms-low crystalline catalysts that possess both stability and excellent HER catalytic activity.

On the other hand, the active sites are the locations where the catalytic reactions occur, and they are the key factor determining the reaction rate and efficiency. The number of active sites is directly related to the catalytic ability of the catalyst. The more active sites there are, the more

[*] Y. Yang⁺, C. Wang⁺, Z. Fu, N. Liu, J. Liu, H. Wu, J. Zheng
 Beijing Advanced Innovation Center for Materials Genome
 Engineering, School of Mathematics and Physics, University of
 Science and Technology Beijing, Beijing 100083, P.R. China
 E-mail: zhengjinlong@ustb.edu.cn

B. Jia
 Key Laboratory of Inorganic Nonmetallic Crystalline and Energy
 Conversion Materials, College of Materials and Chemical
 Engineering, China Three Gorges University, Yichang 443002,
 P.R. China
 E-mail: jiabin1130@126.com

D. Pang⁺
 College of Materials Science & Engineering, Beijing University of
 Technology, Beijing 100124, P.R. China


Z. Guo
 Hebei Key Laboratory of Boron Nitride Micro and Nano Materials,

School of Materials Science and Engineering, Hebei University of
 Technology, Tianjin 300130, P.R. China
 E-mail: zlguo@hebut.edu.cn

X. Fan
 Beijing Key Laboratory for Optical Materials and Photonic Devices,
 Department of Chemistry, Capital Normal University, Beijing 100048,
 P.R. China
 E-mail: fanxiaoyu@cnu.edu.cn

J. Zheng
 Shunde Innovation School, University of Science and Technology
 Beijing, Foshan 528399, P.R. China

[⁺] These authors contributed equally to this work.

 Additional supporting information can be found online in the
 Supporting Information section

reactant molecules can be catalyzed at the same time, thereby significantly increasing the reaction rate.^[12] Doping atoms or creating vacancies is a common method to improve catalyst performance. Heteroatoms, vacancies, or the atoms bonded to them are usually regarded as active sites. This viewpoint has been confirmed in our previous research work. For example, in atomic doping experiments, the Gibbs free energy of H^* (ΔG_{H^*}) of the doped Pt atoms as the active sites was calculated for Pt-doped Ni_5P_4 material. For B-doped Ni_5P_4/Ni_2P material, the B and the connected Ni sites were considered as active sites when performing theoretical calculations.^[13] In vacancy experiments, the Se vacancies were used as the active sites, and the effect of the position of vacancy on the catalytic performance of hydrogen evolution was investigated for the $CoSe_2/MoSe_2$ heterojunction material with Se vacancies ($V_{Se}-CoSe_2/MoSe_2$).^[14] However, when measuring catalytic activity, only limiting single atoms, vacancies or their nearest neighboring atoms as active sites cannot fully show the impact on the overall catalytic activity of the catalyst. This is because the catalyst is a macroscopic whole. And when there is atomic doping or vacancies or both, there are few reports on whether there is an impact on the electronic structure of next-nearest neighbor or more distant atoms. Apart from this, if there is the above-mentioned impact on the electronic structure, the scope of the involved active microscopic region also needs to be further clarified. As a consequence, accurately identifying and locating the active microregions on the catalyst surface has become a key factor in optimizing catalyst performance and developing efficient catalysts.

In this work, a Ru atom-doped low crystalline-crystalline hybrid ($Ru-MoO_{3-x}/Mo_2AlB_2$) is reported as an efficient and stable acidic HER electrocatalyst. By improving the synthesis method, it is possible to synthesize crystalline Mo_2AlB_2 by etching the $MoAlB$ precursor. And at the same time, low crystalline MoO_{3-x} is formed on its surface by spontaneous heat-driven deposition. MoO_{3-x} has the characteristics of short-range order and long-range disorder. And it has a host of O vacancies and other defects, which provides the possibility for the stable doping of Ru atoms. In this study, the short-range ordered atomic array region containing Ru atoms and O vacancies is named as the active microregion for the first time. From an overall perspective, low crystalline $Ru-MoO_{3-x}$ is composed of countless active microregions. The density functional theory calculation results show that the O atoms at the adjacent position of $Ru-O_v-Mo$ have excellent H^* adsorption ΔG_{H^*} as active sites. This is due to the outstanding electron transfer between Ru, Mo, and O, which leads to the optimization of the electronic structure of O. O getting more electrons is more conducive to the conversion of H^+ to H^* . Hence, $Ru-MoO_{3-x}/Mo_2AlB_2$ shows excellent HER catalytic performance. After testing in an acidic electrolyte of 0.5 M H_2SO_4 , the catalyst only needs an overpotential of 38 mV to reach a current density of 10 mA cm^{-2} , and its Tafel slope is 57.1 mV dec^{-1} . Impressively, the performance decay rate is only 0.8% after continuous operation of $Ru-MoO_{3-x}/Mo_2AlB_2$ for 100 h at a voltage of -0.081 V versus RHE. The concept of this new type of atom-doped low crystalline-crystalline hybrid proposed in this study provides a novel method for the synthesis of

electrocatalytic materials. The introduction of the concept of active microregion will also broaden the research ideas of catalytic active sites of catalysts.

Results and Discussion

Morphological and Composition Characterization

In order to realize the construction of a hybrid catalyst with a low crystalline structure on the surface and a crystalline structure inside, and at the same time to avoid the use of highly corrosive HF, a specific synthesis route must be developed to design a customized structure. As shown in Figure 1a, a porous layered structure of MoO_{3-x}/Mo_2AlB_2 was synthesized by alkali hydrothermal etching supplemented by intercalation of an intercalating agent. Then $RuCl_3$ was introduced and instantaneous heating by Joule heat was used to successfully prepare $Ru-MoO_{3-x}/Mo_2AlB_2$.

However, the pore structure and specific surface area of MAB phase materials are relatively limited. During the electrocatalytic reaction process, this may limit the mass transfer and diffusion rates of reactants and products within the catalyst. Moreover, due to the high crystallinity of MAB phase materials, the active sites on their surfaces may be shielded or difficult to access, which in turn affects the overall catalytic performance.^[15] In this work, through a green and efficient etching method, while effectively etching the A layer in MAB, the stability of the material is maintained, and a carrier Mo_2AlB_2 material that can provide metal atoms with abundant active sites is designed. First, using dense layered $MoAlB$, a MAB phase, as the raw material (Figures 1b and S1–S3), the Al layer is etched by NaOH hydrothermal etching. In the MAB phase material $MoAlB$, the Mo–Al bond is a metal bond, while the Mo–B bond is a mixed bond of covalent bond, ionic bond, and metal bond. This leads to a much weaker binding energy strength of Mo–Al, so the Mo–Al bond is more likely to break, and the Al layer is inclined to be etched.^[16–20] As can be seen from the scanning electron microscope (SEM) image of Figure 1c, there is a mass of etched cavities, and an accordion-like layered morphology is maintained. This unique layered structure can increase the specific surface area of the material and increase the area of catalytic reaction sites. As shown in Figure S4, the results of Brunner–Emmet–Teller (BET) measurement indicate that the BET specific surface area of $MoAlB$ is $3.29\text{ m}^2\text{ g}^{-1}$, and the value increases significantly to $11.42\text{ m}^2\text{ g}^{-1}$ after etching and intercalation. The reason for this unique morphology is that the Al layer in the raw material $MoAlB$ is a zigzag double-layer atomic structure. And the etching effect is affected by the defects of the material itself, the Al in the partial area where NaOH is easy to penetrate may be completely etched, while the Al in other areas may be etched off a single layer. There is also an unetched double-layer Al. The possible reaction mechanism in this step is $MoAlB + NaOH \rightarrow Mo_2AlB_2 + NaAlO_2 + H_2O$. Then, using TBAOH as an intercalating agent for intercalation, the MAB structure is further expanded, increasing the specific surface area and the number of pores of the material. At the same

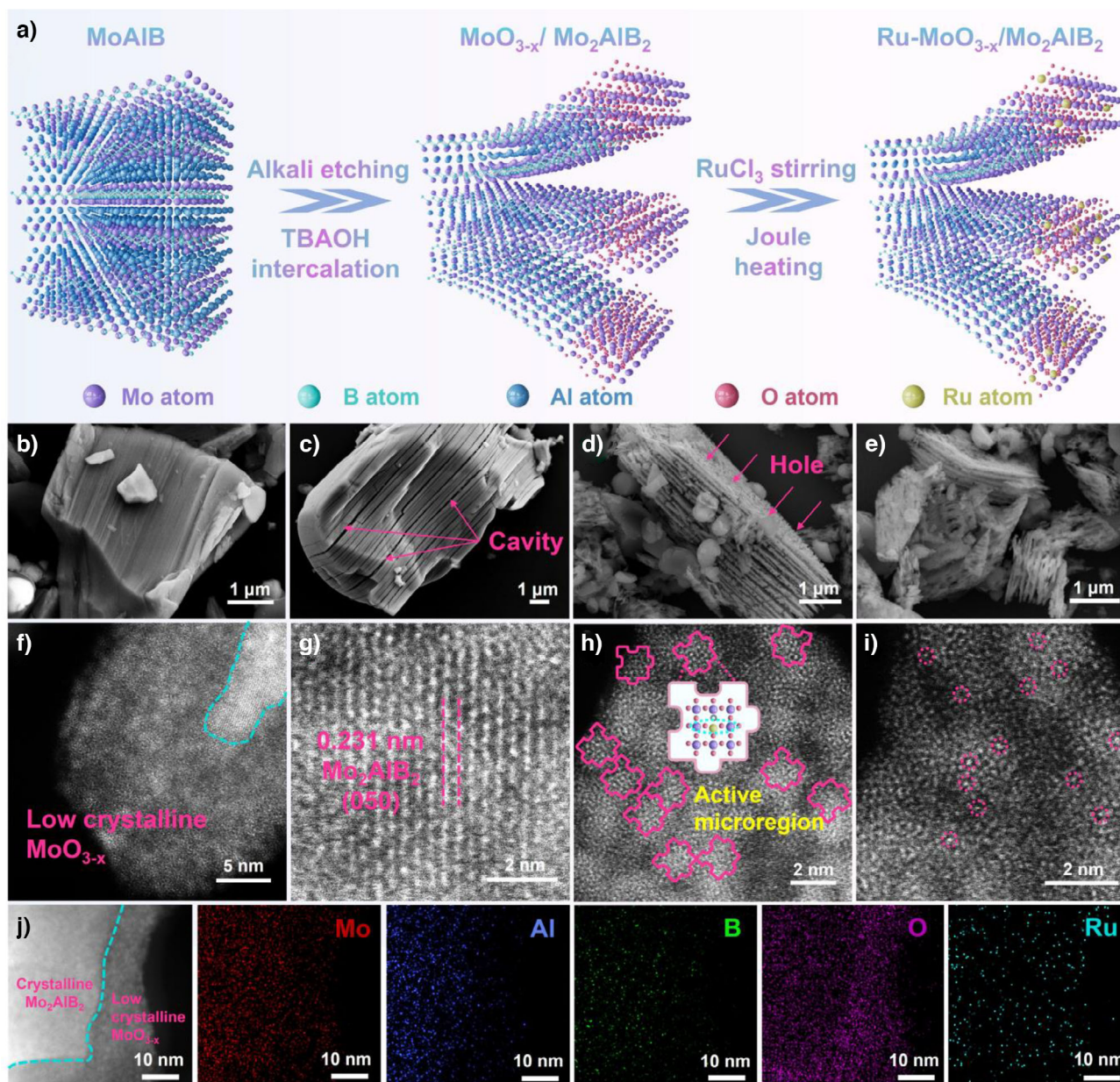


Figure 1. a) Schematic illustration of the structure and synthesis steps of the Ru-MoO_{3-x}/Mo₂AlB₂. SEM image of b) MoAlB, c) Mo₂AlB₂, d) MoO_{3-x}/Mo₂AlB₂, and e) Ru-MoO_{3-x}/Mo₂AlB₂. f-i) AC HAADF-STEM (the jigsaw in the figure is the active microregion). j) HAADF-STEM and EDS mapping of Mo, Al, B, O, and Ru elements of Ru-MoO_{3-x}/Mo₂AlB₂.

time, the surface-active sites of the material increased, and the powder sample with porous layered structure was obtained (Figure 1d).

Subsequently, the powder sample was dispersed in a RuCl₃ aqueous solution, and Ru³⁺ is uniformly adsorbed on the material surface. Due to the intrinsic defects of the material, and as the Mo–Al bond broke during the etching process, some Mo atoms were detached to form Mo vacancies. In order to more fully fix Ru³⁺ at the position of Mo vacancies by means of instantaneous heating strategy, doping of Ru atoms can be achieved without long-term heating and without a strong reducing agent, thus avoiding the enrichment of Ru atoms.^[21,22] As shown in Figures 1e and S5, after the Ru

atoms were fixed by Joule heat, the material morphology still remained excellent. It indicates that the material has excellent thermal stability.

Aberration-corrected high-angle annular dark field (AC-HAADF) images show distinct low crystalline and crystalline dual regions (Figure 1f–i). Among them, a distinct low crystalline region appears on the surface layer of the material with a thickness of approximately more than 10 nm. Besides, a lattice spacing of 0.231 nm can be observed, which matches the (050) crystal plane of Mo₂AlB₂. Since the atomic number of Ru is slightly larger than that of Mo, it will exhibit a higher contrast. It can be observed in Figures 1i and S6 that Ru atoms are distributed both in the external low-crystalline region and

the internal crystalline region, and no Ru clusters or particles are observed, which initially proves the successful doping of Ru atoms.^[23,24] Moreover, the presence of low crystallinity proves that the Joule heat reaction at a lower temperature (650 °C) and for a shorter time can avoid crystallization on the material surface. Relevant research has shown that the electronic state of Ru atomic catalysts is largely related to the local coordination environment between metal atoms and the support.^[25] The MSI of catalysts using low crystalline materials as carriers is often different from that when using crystalline materials as carriers. Specifically, the abundant defects in the low crystalline substrate can effectively anchor Ru atoms and effectively improve the structural stability of Ru atomic catalysts in long-term service environments to achieve high-performance hydrogen evolution reactions. Furthermore, compared to a crystalline substrate, a low crystalline carrier has metal dangling bonds with an unsaturated electronic configuration. Its more frequent orbital coupling redistributes local lone pair electrons and accelerates electron transfer near the active center, optimizing the electronic structure of doped atoms.

It is worth noting that although the low crystalline part presents a disordered atomic structure as a whole, it is arranged regularly according to the crystal configuration in the atomic-level microregion. And it is these numerous microregions arranged regularly that make up the low crystalline part. It is reasonable to speculate that these microregions will influence the overall catalytic activity of the catalyst. Therefore, these regions are named active microregions. In the following, calculations will be carried out on active microregions of different configurations to explore the structure–activity relationship between active microregions and acidic HER catalysis. As shown in Figure 1j, EDS elemental mapping shows that Mo, B, Al, O, and Ru are well dispersed in the internal crystal part, and the content of O element in the low crystalline part on the sample surface is significantly increased, indicating that the surface low crystalline layer may be some kind of oxide. For performance comparison, by controlling the etching time of NaOH, Mo₂AlB₂ without a surface low crystalline structure was also synthesized as a control sample. In terms of morphology, Mo₂AlB₂ also has obvious etched cavities (Figure S7). As shown in Figure S8, inductively coupled plasma emission spectroscopy analysis of MoAlB, Mo₂AlB₂, and Mo₂AlB₂ with a surface rich in low-crystalline oxides confirms the effective etching of Al and the successful doping of Ru, where the mass fraction of Ru is about 7.1 wt%. Compared with the X-ray diffraction (XRD) pattern of MoAlB (Figure S3), as shown in Figure 2a, the peak shoulders of the diffraction peaks of the final sample become broader, which is caused by partial etching. Due to the randomness of the Al etching behavior, not only Mo₂AlB₂ but also a small amount of MoAlB may exist in some regions. The combination of these etched regions and a small amount of unetched regions leads to the broadening of diffraction peaks. These diffraction peaks are highly consistent in position and intensity with the Mo₂AlB₂ XRD card peaks (Table S2) simulated by the calculated lattice constants (Table S1). And it is worth noting that compared with the MoAlB raw

material, the diffraction peak position changes significantly, indicating a clear change in the material composition. In particular, the (020) peak (15.3°) of the final sample in the growth direction shows a shift to a higher angle compared to MoAlB (12.64°). This is because some of the double-layer Al layers have been completely etched, and at the same time, some Al layers change from double layers to single layers, resulting in a shortening of the interlayer spacing. Except for molybdenum oxide, it is not observed in the diffraction pattern, so it can be reasonably considered that molybdenum oxide is not crystalline and only exists on the material surface, which is consistent with the result in Figure 1f. In contrast, as shown in Figure S9, the control sample Mo₂AlB₂ has a relatively stronger (020) diffraction peak, which is attributed to its fully exposed layered surface. As shown in Figure 2b, by comparing the Raman peak positions of the final sample and the sample without Ru atom doping with the Raman peak position of MoAlB, significant differences are found. Regardless of whether Ru atoms are doped or not, synthesized samples show obvious Raman fingerprint peaks of MoO₃ at 279, 661, 818, and 991 cm⁻¹. The strongest Raman peak at 818 cm⁻¹ corresponds to the stretching mode of double-coordinated oxygen (2Mo–O), and the Raman peak at 991 cm⁻¹ corresponds to the stretching mode of Mo⁶⁺–O. What's more, the Raman peaks at 279 and 661 cm⁻¹ correspond to the O=Mo=O double bond and triple-coordinated oxygen (3Mo–O), respectively. Therefore, it is logical to assume that the surface composition of the sample might be MoO₃. It is worth noting that these Raman peaks are more or less broadened, indicating that its lattice structure is distorted, which is consistent with the TEM result. And combined with the electron paramagnetic resonance (EPR) result (Figure 2c), it can be known that when *g* = 2.003, compared with MoAlB, the EPR signal of the final sample is significantly stronger. This is due to the introduction of many O vacancies in the surface molybdenum oxide, confirming the existence of extensive unsaturated metal coordination in the low crystalline substrate. Hence, the final sample is named Ru–MoO_{3-x}/Mo₂AlB₂. This certain amount of oxygen vacancies can effectively improve the conductivity of this metal oxide, thereby further enhancing the HER catalytic performance of this catalytic material.^[4] The short-range ordered and long-range disordered MoO_{3-x} is due to the fact that during the alkaline hydrothermal process, a large amount of Al is removed, and MoAlB gradually transfers to the MoAl_{1-x}B composition. The Mo connected to Al is unstable. Meanwhile, NaOH provides a quantity of –O and –OH groups to the material system. Under the heated ambient temperature, the unstable MoAl_{1-x}B phase is thermally induced to segregate into Mo₂AlB₂ and MoO_{3-x}, and the latter exists on the material surface as a low crystalline form. Mo₂AlB₂ was originally a metastable phase formed during the etching of MoAlB and is prone to phase decomposition. However, with the simultaneous occurrence of Al etching and Mo segregation, a stable MoO_{3-x}/Mo₂AlB₂ hybrid catalyst can finally be formed. Among them, the stable layered structure of Mo₂AlB₂ is like a sturdy skeleton, which can effectively ensure the structural integrity of the catalyst as a whole and provide abundant electron/ion transport channels. The low

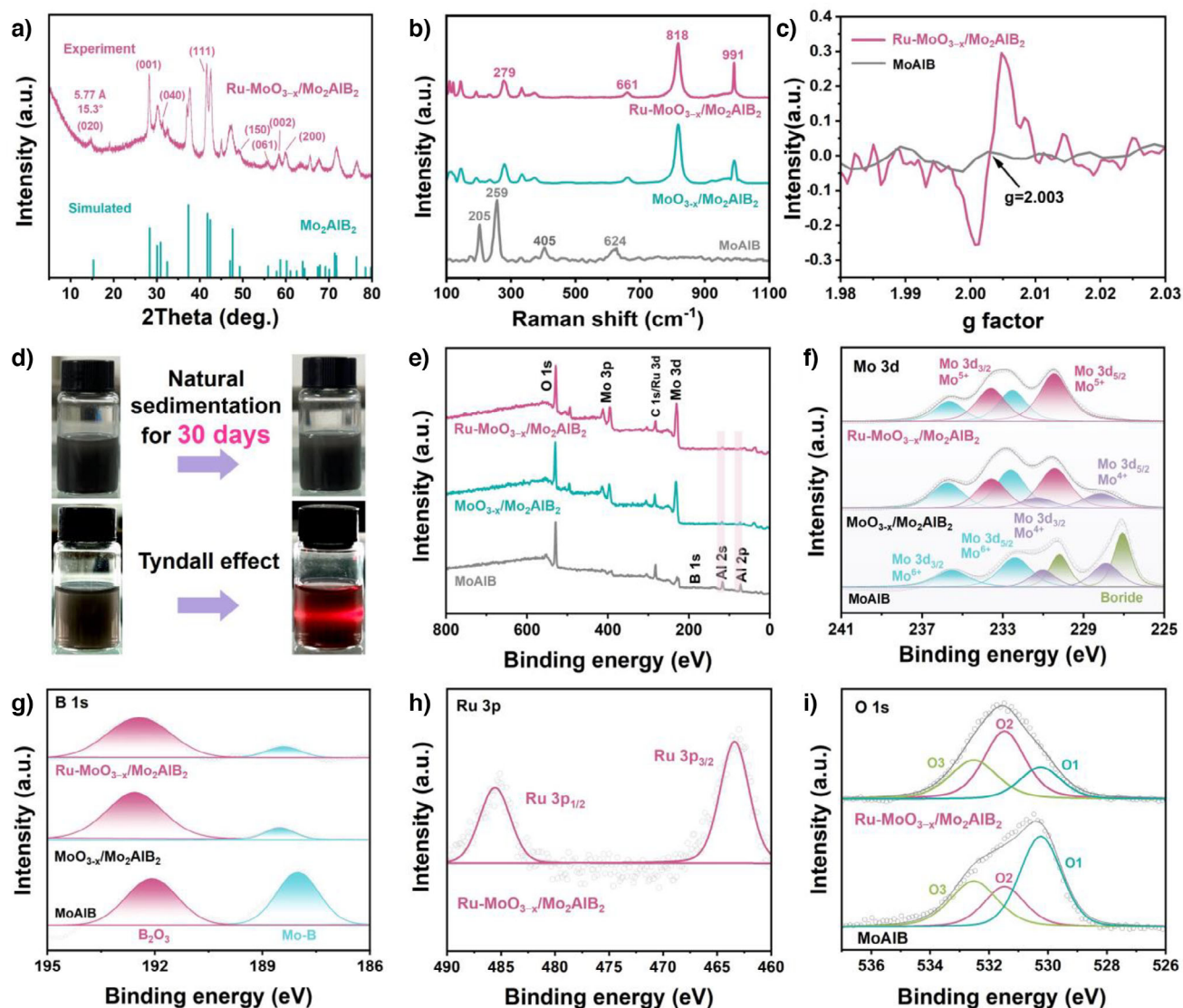


Figure 2. a) XRD patterns of Ru-MoO_{3-x}/Mo₂AlB₂. b) Raman spectra of Ru-MoO_{3-x}/Mo₂AlB₂, MoO_{3-x}/Mo₂AlB₂, and MoAlB. c) EPR spectra of oxygen vacancies of Ru-MoO_{3-x}/Mo₂AlB₂ and MoAlB. d) Natural sedimentation of Ru-MoO_{3-x}/Mo₂AlB₂ solution for 30 days and Tyndall effect diagram for Ru-MoO_{3-x}/Mo₂AlB₂ solution. XPS spectra of the e) survey, f) Mo 3d, g) B 1s, h) Ru 3p, and i) O 1s.

crystalline layer MoO_{3-x} has more defects and vacancies, which can provide more active sites for the catalytic process. In this way, by coupling the layered conductive carrier with the low crystalline active material, it can not only have the high structural stability of the crystal structure but also have the unsaturated electron configuration of the metal suspended bond coordination structure of the low crystalline material to produce a powerful HER catalytic effect. As shown in Figure 2d, the final sample Ru-MoO_{3-x}/Mo₂AlB₂ can be well dispersed in water and ethanol, and there is no obvious sedimentation after standing for 30 days from the macro point of view. Aside from that, the Ru-MoO_{3-x}/Mo₂AlB₂ suspension shows an obvious Tyndall scattering effect and has typical characteristics of uniform colloidal dispersion.

X-ray photoelectron spectroscopy (XPS) reveals the electron transfer situation of Mo. The spectrum of survey (Figure 2e) shows that after etching by NaOH, the relative

intensity of the Al element peak of the MoO_{3-x}/Mo₂AlB₂ sample is significantly lower than that of the MoAlB sample, which means that Al is effectively removed. And Figure S10 shows the fine spectrum of Al. In the Mo 3d spectrum (Figure 2f), the MoAlB raw material shows obvious boride peaks, while the Mo-B peak does not appear in MoO_{3-x}/Mo₂AlB₂. This is because the detection depth of XPS is limited and only the signal of low crystalline MoO_{3-x} on the material surface can be detected. It is worth noting that after the introduction of Ru atoms, the Mo⁴⁺ peak disappears and the binding energy of Mo moves to a higher value, showing two higher valence states of +5 and +6. This initially confirms that Mo has successfully lost some electrons. In addition, as shown in Figure 2g, B1s is fitted by Mo-B and B₂O₃. When low-crystalline MoO_{3-x} appears on the material surface, the intensity of the Mo-B peak is significantly reduced and the peak almost disappears, further

proving the successful synthesis of MoO_{3-x} on the material surface. The characteristic peak of Ru 3p (Figure 2h) shows the successful doping of Ru.^[26] Combined with Figure 1g, Ru atoms are distributed not only in the surface low crystalline region but also in the internal crystal. According to analysis, the successful doping of Ru is related to both spontaneous redox and Joule heat fixation. First, the long-range disordered low-crystalline MoO_{3-x} on the surface of the hybrid catalyst is rich in numerous Mo and O defects, providing satisfactory conditions for the doping of Ru. For the internal Mo_2AlB_2 crystal, during the etching process of MoAlB by NaOH, some Mo connected to Al is also etched together, and Mo single vacancies or vacancy clusters will also be formed. Whether it is the Mo vacancies on the inside or the surface, they are reactive (showing reducibility), and Ru^{3+} has a certain oxidizing property.

Consequently, there is an oxidation-reduction force for adsorption when the two come into contact, and a reaction occurs to reduce Ru^{3+} . This process can be named as the simultaneous self-reduction stabilization process. Finally, supplemented by the instantaneous heating process of Joule heat, a thermal shock was applied to the material. The energy provided by this low-temperature instantaneous thermal shock enables Ru atoms to form stable bonds with the substrate and avoids the damage to the low-crystalline matrix caused by long-term high-temperature synthesis. As shown in Figure 2i, the XPS spectrum of O 1s can be divided into three peaks, from low binding energy to high binding energy, which are the peak of Mo–O bond, O vacancy, and adsorbed O. After comparison, it is found that the peak area of oxygen vacancies in the $\text{Ru–MoO}_{3-x}/\text{Mo}_2\text{AlB}_2$ sample is significantly larger than that in MoAlB , attributing to abundant O vacancies in the low crystalline MoO_{3-x} on the sample surface.^[27]

To further explore the microscopic bond structure of the material, X-ray absorption spectroscopy characterization was carried out on this material. As shown in Figure 3a, the X-ray absorption near-edge spectroscopy (XANES) shows that the edge energy in the Ru K-edge XANES spectrum of the final sample $\text{Ru–MoO}_{3-x}/\text{Mo}_2\text{AlB}_2$ is between Ru foil and RuO_2 , proving that the valence state of Ru is between 0 and +4.^[28] And from the X-ray absorption fine structure spectrum (EXAFS) of Ru (Figure 3b), it can be clearly found that there is a quite obvious Ru–O peak at 1.47 Å in the $\text{Ru–MoO}_{3-x}/\text{Mo}_2\text{AlB}_2$ sample. It is worth noting that a signal peak of Ru–O–Mo appears at 3.02 Å. As shown in Figure 3d–f, the wavelet transform (WT) of the Ru K-edge EXAFS of the $\text{Ru–MoO}_{3-x}/\text{Mo}_2\text{AlB}_2$ sample clearly shows that the main peak at 5 Å^{-1} is similar to the WT of the K-edge EXAFS of RuO_2 . This is attributed to Ru–O coordination. And there is no Ru–Ru coordination in the final sample, indicating the successful dispersive formation of Ru atoms. What's more, in the Mo K-edge XANES spectrum (Figure 3c), it can be found that the oxidation state of Mo in $\text{Ru–MoO}_{3-x}/\text{Mo}_2\text{AlB}_2$ is between MoO_2 and MoO_3 , and the Mo valence state in $\text{Ru–MoO}_{3-x}/\text{Mo}_2\text{AlB}_2$ is higher than that in $\text{MoO}_{3-x}/\text{Mo}_2\text{AlB}_2$.^[29] This indicates that after the introduction of Ru atoms, Mo atoms show obvious electron donor characteristics. As shown in Figure S11, the

EXAFS of Mo shows that there is an obvious Mo–Mo signal in $\text{MoO}_{3-x}/\text{Mo}_2\text{AlB}_2$. However, after doping Ru, the Mo–Mo peak of $\text{Ru–MoO}_{3-x}/\text{Mo}_2\text{AlB}_2$ shows a slight left shift. This may be due to some Ru atoms occupying the position of Mo. As shown by the WT of Mo (Figure S12), there are obvious Mo–Mo and Mo–O–Ru signals in $\text{Ru–MoO}_{3-x}/\text{Mo}_2\text{AlB}_2$, which is consistent with the XANES result of Ru, once again confirming the successful doping of Ru. Furthermore, compared with $\text{MoO}_{3-x}/\text{Mo}_2\text{AlB}_2$, the peak intensity in k-space of Mo in the final sample is slightly reduced (Figure S13), indicating that after the introduction of Ru, the lattice distortion and coordination shell of Mo are slightly reduced.

Considering that catalytic reactions usually take place on the surface of the catalyst, the bonds on the catalyst surface are of great significance for research. Now, the research object is shifted from the entire catalyst to the surface region of the catalyst where catalytic reactions occur, namely Ru–MoO_{3-x} . The regions without O vacancies and Ru atoms and those with O vacancies and Ru atoms are respectively calculated and simulated to compare the changes in bond lengths. Combined with the calculation modeling results (Figure S14), Figure 3g illustrates in a schematic diagram that the Ru–O–Mo bonding and Mo–O–Mo bonding in the active microregion accelerate HER kinetics through the shortened O–Mo path. Specifically, for original MoO_3 , the bond length of Mo–O–Mo is 3.63 Å (the Mo–O bond length is 1.93 Å, and the Mo–O–Mo bond angle is 139.6°). After the introduction of oxygen vacancies and ruthenium atoms, the bonding situation near the oxygen vacancies changes. At this time, the bond length of Ru–O–Mo is shortened to 3.57 Å (the Mo–O bond length is 1.89 Å, the Ru–O bond length is 1.93 Å, and the Ru–O–Mo bond angle is 138.8°). Previously, for catalysts loaded with noble metal atoms, it was generally the regular structural coordination and coupling between the noble metal atoms and the nonmetal atoms of the substrate. Generally, the bond lengths are relatively long, making it difficult to adjust the electronic states of the metal atoms, which leads to a significant reduction in the catalytic activity of the atoms. In this study, due to the existence of a large amount of O vacancy defects in low crystalline MoO_{3-x} , a more affine coordination structure is formed between precious metal atoms and substrate metal atoms. This coordination structure is conducive to electron transfer between Ru, Mo, and O atoms, further regulating the electronic configuration of local O sites and helping to accelerate the HER reaction kinetics.

Electrocatalytic Performance

Hydrogen evolution performance tests were carried out on the synthesized final sample $\text{Ru–MoO}_{3-x}/\text{Mo}_2\text{AlB}_2$ and its control samples MoAlB , Mo_2AlB_2 , and $\text{MoO}_{3-x}/\text{Mo}_2\text{AlB}_2$ under a standard three-electrode system. In an acidic medium, the high concentration of protons makes proton transfer easier and greatly accelerates the reaction rate, which is crucial for application scenarios that pursue high production capacity and rapid reaction. Hence, the chosen test environment is an acidic electrolyte of 0.5 M H_2SO_4 . As shown in Figure 4a,

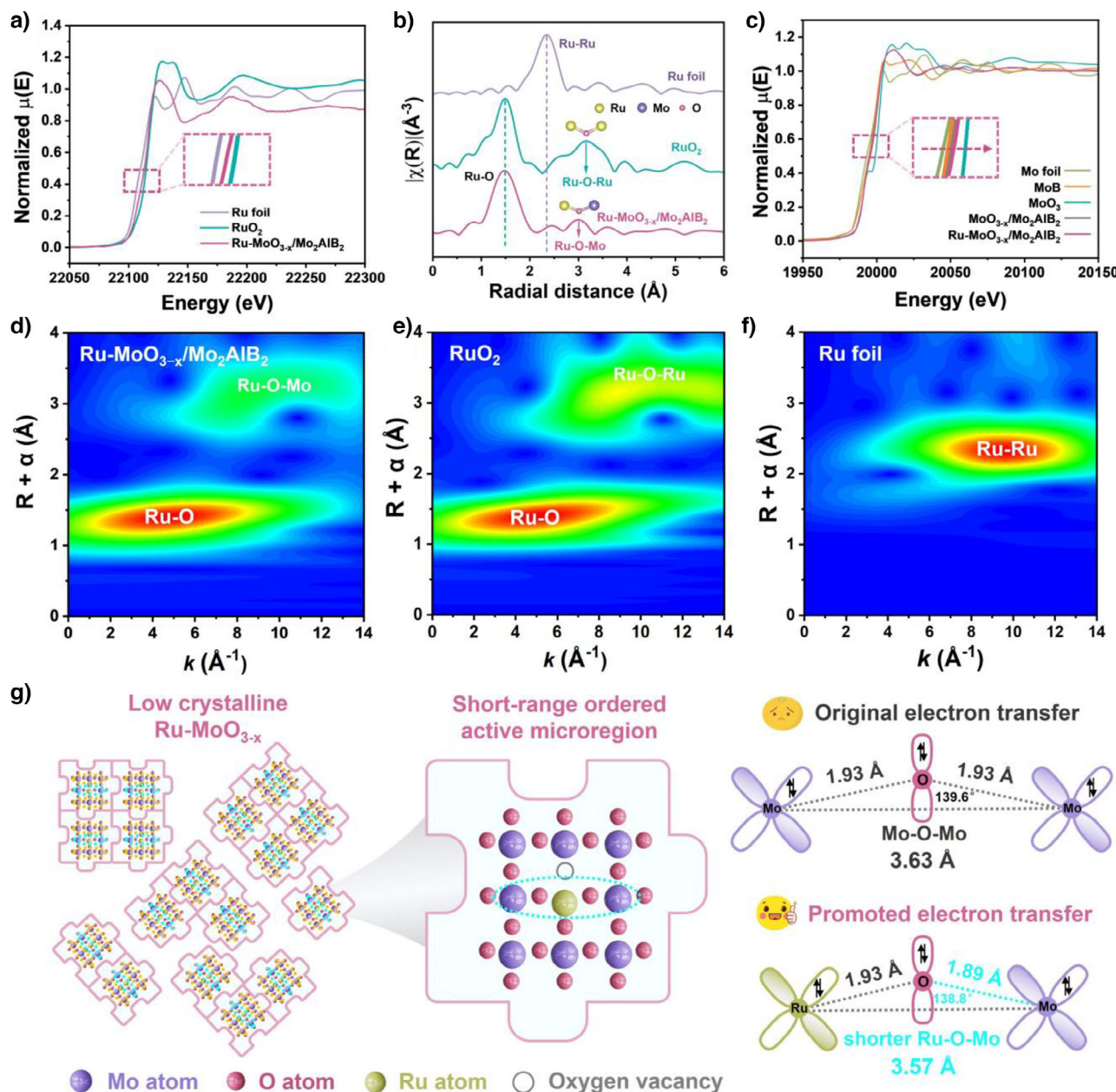


Figure 3. a) Ru K-edge XANES. b) Ru K-edge FT-EXAFS. c) Mo K-edge XANES, WT for the k^3 -weighted EXAFS spectra of the Ru K-edge in d) Ru-MoO_{3-x}/Mo₂AlB₂, e) RuO₂, and f) Ru foil. g) Schematic description of the electronic coupling among Ru-O-Mo bridge and Mo-O-Mo bridge.

the doping of Ru atoms endows Ru-MoO_{3-x}/Mo₂AlB₂ with the best catalytic activity. It only needs an overpotential of 38 mV to reach a current density of 10 mA cm⁻². Significantly better than MoAlB (445 mV), Mo₂AlB₂ (252 mV), and MoO_{3-x}/Mo₂AlB₂ (75 mV). In Figure 4b, the Tafel slope of Ru-MoO_{3-x}/Mo₂AlB₂ is 57.1 mV dec⁻¹, which is much lower than that of MoAlB (167.5 mV dec⁻¹), Mo₂AlB₂ (156.7 mV dec⁻¹), and MoO_{3-x}/Mo₂AlB₂ (77.9 mV dec⁻¹), indicating that Ru-MoO_{3-x}/Mo₂AlB₂ has more excellent Volmer-Heyrovsky reaction kinetics,^[30] which is caused by the electronic regulation among Ru atoms, Mo atoms, and O atoms. Electrochemical impedance spectroscopy measurement was performed on the catalyst to detect its

intrinsic resistance and kinetic properties (Figure 4c). Measured at a voltage of -0.001 V versus RHE and fitted with an equivalent circuit.^[31] The results show that Ru-MoO_{3-x}/Mo₂AlB₂ has the smallest charge transfer resistance (R_{ct}) of 3.5 Ω (Figure S15). The strong metal-support interaction between the low crystalline MoO_{3-x} substrate and Ru atoms endows Ru-MoO_{3-x}/Mo₂AlB₂ with faster electron transfer and enhanced reaction kinetics. The double-layer capacitance (C_{dl}) is calculated according to the cyclic voltammetry curves measured in the non-Faraday region (Figure S16).^[32] As shown in Figure 4d, the C_{dl} of the final sample Ru-MoO_{3-x}/Mo₂AlB₂ is the largest, being 27 mF cm⁻², which is significantly greater than that of

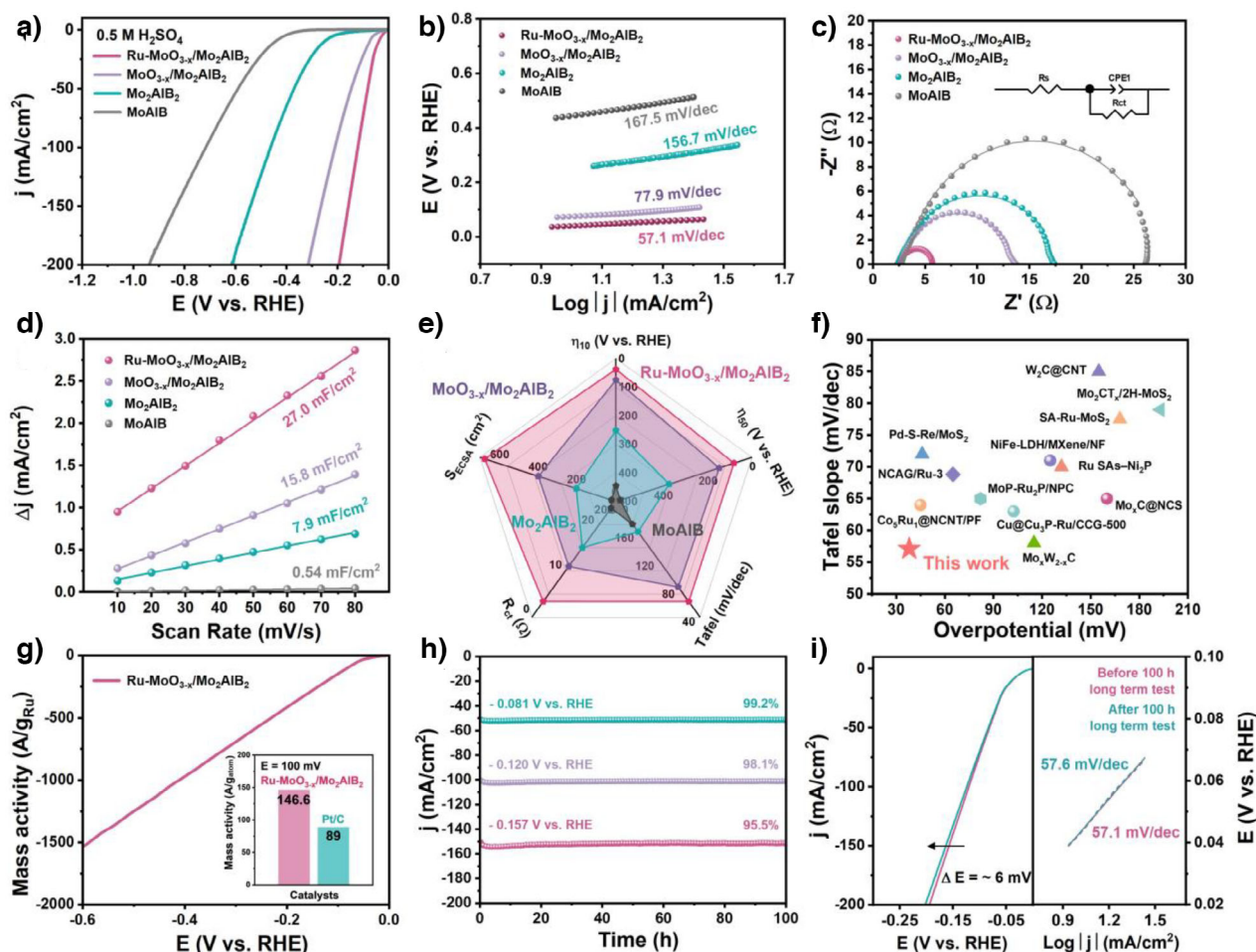


Figure 4. a) HER polarization curves for Ru-MoO_{3-x}/Mo₂AlB₂, MoO_{3-x}/Mo₂AlB₂, Mo₂AlB₂, and MoAlB at a scan rate of 1 mV s⁻¹ in 0.5 M H₂SO₄. b) Corresponding Tafel diagrams. c) Nyquist plots. d) C_{dl} values of different samples. e) Comparison of various properties of the Ru-MoO_{3-x}/Mo₂AlB₂, MoO_{3-x}/Mo₂AlB₂, Mo₂AlB₂, and MoAlB catalysts. f) Reported overpotentials versus Tafel slopes for different catalysts. g) Mass activity curve of Ru-MoO_{3-x}/Mo₂AlB₂ and the mass activity value of Ru atom in Ru-MoO_{3-x}/Mo₂AlB₂ and Pt atom in Pt/C at 100 mV. h) 100 h long-term *i*-*t* tests of Ru-MoO_{3-x}/Mo₂AlB₂ in 0.5 M H₂SO₄ electrolyte. i) LSV curves and Tafel slopes of Ru-MoO_{3-x}/Mo₂AlB₂ before and after 100 h long-term test.

MoO_{3-x}/Mo₂AlB₂ and other control samples, indicating that the addition of Ru atoms provides abundant active sites for the catalyst. The corresponding electrochemical surface area (ECSA) value of the catalyst is calculated to study the source of the superior activity of the synthesized catalyst, according to the formula $ECSA = C_{dl}/C_s$. As shown in Figure S17, compared with MoAlB (13.5 cm²), Mo₂AlB₂ (197.5 cm²), and MoO_{3-x}/Mo₂AlB₂ (395 cm²), the ECSA of Ru-MoO_{3-x}/Mo₂AlB₂ is as high as 675 cm², indicating that the construction of surface low crystalline MoO_{3-x} can effectively increase the number of active sites.^[33,34] From an overall perspective, Ru-MoO_{3-x}/Mo₂AlB₂ shows excellent catalytic activity in the acidic HER process (Figure 4e). In particular, the HER activity of this unique Ru-doped low crystalline MoO_{3-x}/crystalline Mo₂AlB₂ hybrid catalyst is superior to most transition metal-based material HER catalysts and Ru-containing HER catalysts (Figure 4f and Table S3). Apart from this, the mass activity (MA) test was performed on the catalyst, and the MA of Ru-MoO_{3-x}/Mo₂AlB₂ and commer-

cial Pt/C catalyst at 100 mV was compared.^[4,35] The results in Figure 4g show that the MA of Ru-MoO_{3-x}/Mo₂AlB₂ is 146.6 A g_{Ru}⁻¹, which is 1.6 times that of the commercial Pt/C catalyst. The Ru-MoO_{3-x}/Mo₂AlB₂ catalyst system shows outstanding catalytic stability. Voltages of -0.081 V versus RHE, -0.120 V versus RHE, and -0.157 V versus RHE are applied to it, respectively. As shown in Figure 4h, after continuous operation for 100 h, the activity retention rates of the Ru-MoO_{3-x}/Mo₂AlB₂ catalyst are still as high as 99.2%, 98.1%, and 95.5%, respectively. This is because Mo₂AlB₂ acts like a skeleton with a layered porous structure in the overall catalyst, and it has strong crystallinity. It complements the low-crystalline structure of MoO_{3-x} on the surface, thus ensuring the overall stability of the catalyst in the acidic electrolyte. Accordingly, Ru-MoO_{3-x}/Mo₂AlB₂ has outstanding development potential. And as can be seen from the LSV curves before and after the test (Figure 4i), when the current density reaches 150 mA cm⁻², the potential difference is only about 6 mV. Also, the Tafel slope changes from

the original 57.1 to 57.6 mV dec⁻¹, with almost no change. Finally, a series of characterizations were carried out on Ru–MoO_{3-x}/Mo₂AlB₂ after the long-term HER tests. From a microscopic structure perspective (Figure S18), the morphologies of all samples did not change significantly after the HER test, and the structure remained good. In addition to the morphology, as shown in Figures S19–S21, the composition of Ru–MoO_{3-x}/Mo₂AlB₂ did not change before and after the reaction. In short, since the crystal substrate (Mo₂AlB₂) has a stable layered structure, it lays a strong foundation for Ru–MoO_{3-x}/Mo₂AlB₂ to have marvelous performance stability and a wide range of voltage applicability. Furthermore, the high activity and stability of Ru–MoO_{3-x}/Mo₂AlB₂ can be attributed to the atomic-level dispersion of Ru on the hybrid substrate and is stabilized by the Ru–O–Mo bond with a shortened bond length. The porous layered hybrid of MoO_{3-x}/Mo₂AlB₂ with a large specific surface area also provides more active sites for electrochemical HER.

Theoretical Calculations

To deeply explore the intrinsic relationship between the low crystalline active microregion on the surface of Ru–MoO_{3-x}/Mo₂AlB₂ and the high HER catalytic activity, relevant theoretical calculations were carried out using first principles.^[36–38] Since MoO_{3-x} possesses a layered structure, the surface atoms are selected as the calculation object. Recalling the concept of active microregion mentioned above, it is assumed that the catalyst as a whole is composed of countless tiny active microregions, each exhibiting different configurations. So which configuration will make outstanding contributions to the overall catalytic activity of the catalyst? Keeping this thought in mind, four types of active microregion models (Figures 5a–d and S22) were established, with the presence or absence of O vacancies and the doping of Ru atoms serving as variables. It can be found that when only O vacancies are introduced, there is no obvious change in the structure as a whole. But the Mo connected to the O vacancies repels each other, resulting in a shortening of the Mo–O–Mo bond length and a change in the bond angle near the O vacancies (Figure 5b). Similarly, after the introduction of Ru atoms alone, there is no apparent disturbance in the structure. In order to further evaluate the stability of the system, *ab initio* molecular dynamics (AIMD) simulations were carried out on the systems before and after Ru doping (Figure S23). The simulations were conducted at 300 K for a duration of 10 ps. The results indicate that on the time scale of 10 000 fs in the AIMD simulations, the atoms merely vibrate slightly around their equilibrium positions, with no observable structural collapse or decomposition, which demonstrates their thermodynamic stability at room temperature. This also indirectly verifies the reliability of doping Ru in the experiment that Ru atoms can exist by replacing Mo atoms (Figure 5c). In addition, different doping positions of Ru relative to O vacancies were also calculated. As shown in Figure S24, when the Ru atom is situated at the nearest neighbor position of the oxygen vacancy, the calculation results demonstrate that the system energy is the

lowest, suggesting the better stability of this configuration. This also implies that Ru has an inherent selectivity for doping at the nearest neighbor position of the oxygen vacancy. Therefore, the configuration depicted in Figure 5d is selected as the favorable configuration for the coexistence of oxygen vacancy and single Ru atom. Because of the absolute value of ΔG_{H^*} can evaluate the HER performance of catalysts.^[39,40] Calculations have been carried out on partial Mo sites, Ru sites, and O sites within the four types of microregions (Figures 5a–d and S25). Surprisingly, different from the conventional situation where metals are the active sites for hydrogen evolution, the ΔG_{H^*} of Mo and Ru in the four configurations is too large, and it can be considered that they do not have excellent ability to adsorb H^{*}. However, the results show that the O atoms adjacent to Ru–O_v–Mo in microregion 4 (sites I–III) show the ΔG_{H^*} closest to 0, which are 0.06 eV (site I), –0.09 eV (site II), and 0.02 eV (site III), respectively, indicating that the O active sites of this region have strong hydrogen evolution potential. In addition to these adjacent O sites, the ΔG_{H^*} of some O atoms in microregion 4 was also calculated, and the ΔG_{H^*} of all calculated O sites was summarized (Figure 5e). On the whole, the ΔG_{H^*} of O sites is generally excellent. As shown in Figure 5f, in order to screen the optimal active microregion configuration, a comparison was made of the catalytic activity of the best hydrogen evolution active sites in the four microregions and found that site III in microregion 4 has the best ΔG_{H^*} . It shows a moderate adsorption and desorption ability. As a result, it can be considered that this active microregion, characterized by the presence of both O vacancies and Ru atoms, is crucial for the catalyst to demonstrate outstanding overall catalytic hydrogen evolution performance. Looking at the differential charge density of the O sites with the best binding energy in four microregions (Figures 5g and S26), the O site in microregion 4 shows the optimal electron accumulation state. It is proved that the formation of O vacancies and the doping of Ru atoms are both conducive to the accumulation of electrons at O sites, which is helpful for the subsequent adsorption of H^{*} and the release of H₂. In addition, the results of the electron localization function (ELF), as shown in Figure S27, indicate that the region around the O atom exhibits a high electron density, while the local electron densities of Ru and Mo are relatively low. This also suggests that the surface electrons are transferred from the Ru and Mo atoms to the O atoms. Furthermore, the Bader charges of these O sites with the best H^{*} adsorption free energy and their surrounding Mo and Ru sites were calculated (Figure 5h and Table S4). The results are consistent with the results of differential charge density. The O in microregion 4 is more inclined to obtain electrons from Mo and Ru (Bader charge values of O sites in microregion 1: 0.99 |e|, in microregion 2: 1.02 |e|, in microregion 3: 0.98 |e|, and in microregion 4: 1.03 |e|). This is because the original single-layer MoO₃ structure is a net-like structure, doping of Ru atoms and the introduction of oxygen vacancies lead to an increase in the local electron density near the oxygen vacancy itself. Therefore, the bonding length of Ru–O–Mo around the oxygen vacancy is shorter than that of Mo–O–Mo in the absence of oxygen vacancies and Ru atoms (it shortens

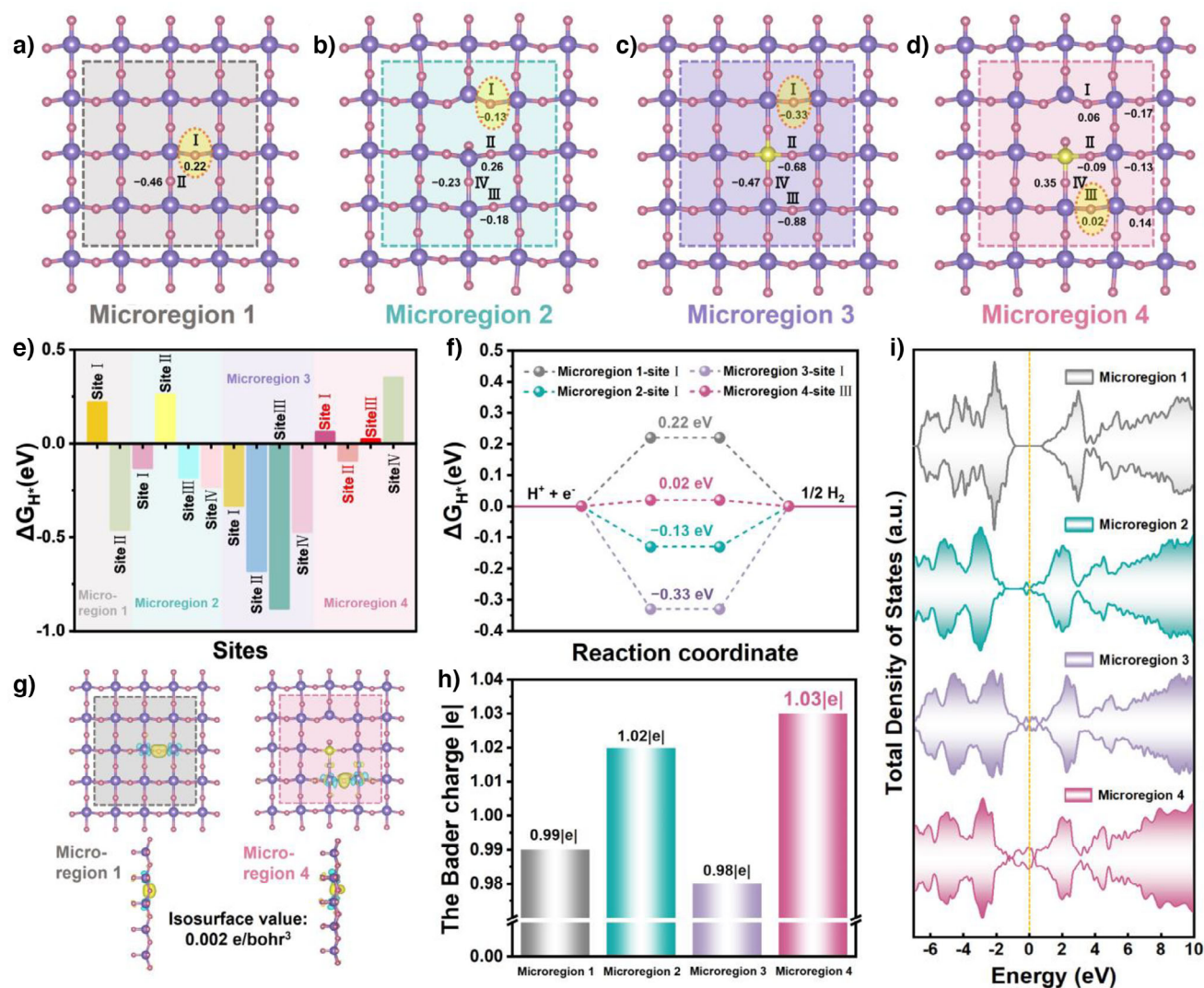


Figure 5. a–d) ΔG_{H^*} values of O sites in microregion 1, microregion 2, microregion 3, and microregion 4. e) ΔG_{H^*} values of different sites of microregion 1–microregion 4. f) ΔG_{H^*} values of the best sites within each microregion. g) The front view and side view of differential charge density of the best O sites in microregion 1 and microregion 4. h) Bader charge values of O sites in microregion 1–microregion 4. i) TDOS of microregion 1–microregion 4 (purple balls: Mo atoms, pink balls: O atoms, and yellow balls: Ru atoms).

from 3.63 Å for Mo–O–Mo to 3.57 Å for Ru–O–Mo), and the bond angle is also reduced (it decreases from 139.6° for Mo–O–Mo to 138.8° for Ru–O–Mo). The shorter bonding makes the bond stronger, and then accelerates the electron transfer from Ru to O and from Mo to O. This efficient electron transfer can help optimize the local electronic configuration of O atoms, help O atoms accumulate more electrons, facilitate the combination with H^+ to form H^* , and further accelerate the HER kinetics of the catalyst. Furthermore, using O as the active site has another prominent advantage. In the surface low crystalline Ru–MoO_{3-x}, the number of active O sites is quite large, whether it is for Mo or the sporadically distributed Ru. As a consequence, it is easier to improve the overall catalytic hydrogen evolution activity of the catalyst by adjusting the electronic structure of O. In addition, in Figure 5i, the calculation results of the total density of states

(TDOS) of the four active microregions show that after the introduction of Ru atoms or O vacancies, the bandgap disappears, and the properties of the material change from those of a semiconductor to those of a conductor. Moreover, the density of states at the Fermi level in microregion 4 is the highest, exhibiting the highest electrical conductivity, which is beneficial for electron transfer during the electrocatalytic process. As a supplement, considering the strong correlation effect of the d electrons of transition metals, the density of states (DOS) of the four microregions was calculated using the HSE06 functional (Figure S28). The results show that the bandgap calculated by the HSE functional is wider than that calculated by the PBE functional. Moreover, the variation patterns of the DOS of different microregions calculated by HSE are basically the same as those calculated by PBE. This reflects the reliability of the calculation results.

To sum up, four possible microscopic configurations within catalysts have been studied and named active microregions. In the active microregion with O vacancy and Ru atom, the synergistic effect of O vacancy and Ru atom leads to the change of bonding structure. In particular, the bond length is shortened, which is conducive to the modulation of the electronic structure, and then helps O accumulate more electrons. And in the microregion 4, many O sites all show excellent ΔG_{H^*} . The existence of these highly active O sites breaks through the conceptual constraint of only taking a single precious metal site as the hydrogen evolution active site. At the same time, each O site undergoes the catalytic process simultaneously, thereby significantly improving the overall catalytic efficiency of the catalyst.

Conclusion

In conclusion, a new type of Ru atom-doped crystal-low crystalline hybrid, $\text{MoO}_{3-x}/\text{Mo}_2\text{AlB}_2$, has been successfully designed and defined the atomic-level array rich in Ru atoms and O vacancies in the low crystalline part as the active microregion. The Ru—O—Mo with shortened bond lengths inside the active microregion provides a satisfactory prerequisite for the modulation of the electronic structure of O. The formation of this electron-rich O atom is the key active source of the active microregion. Judging from the results, the $\text{Ru—MoO}_{3-x}/\text{Mo}_2\text{AlB}_2$ catalyst only needs an overpotential of 38 mV to reach a current density of 10 mA cm^{-2} , showing excellent HER catalytic activity. At the same time, due to the existence of the crystal-low crystalline hybrid structure configuration, the catalyst can operate stably for more than 100 h at different voltages. This work reveals the specific configuration, electronic state, and structure–activity relationship of the local microenvironment of the catalyst active region on the scale of active microregions, opening up a novel path for in-depth understanding of the catalytic mechanism and optimizing the design of efficient catalysts.

Acknowledgements

This work was financially supported by the National Natural Science Foundation of China (52271200) and the Guangdong Basic and Applied Basic Research Foundation (2024A1515010393). The computing work is supported by USTB MatCom of Beijing Advanced Innovation Center for Materials Genome Engineering.

Conflict of Interests

The authors declare no conflict of interest.

Data Availability Statement

The data that support the findings of this study are available from the corresponding author upon reasonable request.

Keywords: Acid hydrogen evolution reaction • Active microregion • Atom doping • Oxygen vacancy

- [1] J. Chen, M. Aliasgar, F. B. Zamudio, T. Zhang, Y. Zhao, X. Lian, L. Wen, H. Yang, W. Sun, S. M. Kozlov, W. Chen, L. Wang, *Nat. Commun.* **2023**, *14*, 1711.
- [2] B. Pang, X. Liu, T. Liu, T. Chen, X. Shen, W. Zhang, S. Wang, T. Liu, D. Liu, T. Ding, Z. Liao, Y. Li, C. Liang, T. Yao, *Energy Environ. Sci.* **2022**, *15*, 102–108.
- [3] B. Zeng, X. Liu, L. Wan, C. Xia, L. Cao, Y. Hu, B. Dong, *Angew. Chem. Int. Ed.* **2024**, *63*, e202400582.
- [4] C.-A. Zhou, K. Ma, Z. Zhuang, M. Ran, G. Shu, C. Wang, L. Song, L. Zheng, H. Yue, D. Wang, *J. Am. Chem. Soc.* **2024**, *146*, 21453–21465.
- [5] X. Chen, X.-T. Wang, J.-B. Le, S.-M. Li, X. Wang, Y.-J. Zhang, P. Radjenovic, Y. Zhao, Y.-H. Wang, X.-M. Lin, J.-C. Dong, J.-F. Li, *Nat. Commun.* **2023**, *14*, 5289.
- [6] Y. Zhu, M. Klingenhof, C. Gao, T. Koketsu, G. Weiser, Y. Pi, S. Liu, L. Sui, J. Hou, J. Li, H. Jiang, L. Xu, W.-H. Huang, C.-W. Pao, M. Yang, Z. Hu, P. Strasser, J. Ma, *Nat. Commun.* **2024**, *15*, 1447.
- [7] L. Zeng, Z. Zhao, Q. Huang, C. Zhou, W. Chen, K. Wang, M. Li, F. Lin, H. Luo, Y. Gu, L. Li, S. Zhang, F. Lv, G. Lu, M. Luo, S. Guo, *J. Am. Chem. Soc.* **2023**, *145*, 21432–21441.
- [8] W. Chen, M. Yu, S. Liu, C. Zhang, S. Jiang, G. Duan, *Adv. Funct. Mater.* **2024**, *34*, 2313307.
- [9] L. Wang, M. Ma, C. Zhang, H. H. Chang, Y. Zhang, L. Li, H. Y. Chen, S. Peng, *Angew. Chem. Int. Ed.* **2024**, *63*, e202317220.
- [10] J. Xu, H. Jin, T. Lu, J. Li, Y. Liu, K. Davey, Y. Zheng, S. Qiao, *Sci. Adv.* **2023**, *9*, eadh1718.
- [11] Y. Zhou, W. Hao, X. Zhao, J. Zhou, H. Yu, B. Lin, Z. Liu, S. J. Pennycook, S. Li, H. Fan, *Adv. Mater.* **2022**, *34*, 2100537.
- [12] I. Ro, J. Qi, S. Lee, M. Xu, X. Yan, Z. Xie, G. Zakem, A. Morales, J. G. Chen, X. Pan, D. G. Vlachos, S. Caratzoulas, P. Christopher, *Nature* **2022**, *609*, 287–292.
- [13] M. Sun, H. Wang, H. Wu, Y. Yang, J. Liu, R. Cong, Z. Liang, Z. Huang, J. Zheng, *Dalton Trans.* **2024**, *53*, 3559–3572.
- [14] K. Wu, C. Wang, X. Lang, J. Cheng, H. Wu, C. Lyu, W.-M. Lau, Z. Liang, X. Zhu, J. Zheng, *J. Colloid Interface Sci.* **2024**, *654*, 1040–1053.
- [15] Z. Guo, J. Zhou, Z. Sun, *J. Mater. Chem. A* **2017**, *5*, 23530–23535.
- [16] M. Ade, H. Hillebrecht, *Inorg. Chem.* **2015**, *54*, 6122–6135.
- [17] P. Helmer, J. Halim, J. Zhou, R. Mohan, B. Wickman, J. Björk, J. Rosen, *Adv. Funct. Mater.* **2022**, *32*, 2109060.
- [18] Z. Wang, J. Su, D. Feng, Y. Yao, Y. Yan, Y. Cui, G. M. Rignanese, H. Hosono, J. Wang, *Small* **2024**, *20*, 2407100.
- [19] Q. Shen, Y. Shi, Y. He, J. Wang, *Adv. Sci.* **2024**, *11*, 2308589.
- [20] L. T. Alameda, P. Moradifar, Z. P. Metzger, N. Alem, R. E. Schaak, *J. Am. Chem. Soc.* **2018**, *140*, 8833–8840.
- [21] Z. Zhao, J. Sun, X. Li, S. Qin, C. Li, Z. Zhang, Z. Li, X. Meng, *Nat. Commun.* **2024**, *15*, 7475.
- [22] G. He, M. Yan, H. Gong, H. Fei, S. Wang, *Int. J. Extrem. Manuf.* **2022**, *4*, 032003.
- [23] A. R. Poerwoprajitno, L. Gloag, J. Watt, S. Cheong, X. Tan, H. Lei, H. A. Tahini, A. Henson, B. Subhash, N. M. Bedford, B. K. Miller, P. B. O'Mara, T. M. Benedetti, D. L. Huber, W. Zhang, S. C. Smith, J. J. Gooding, W. Schuhmann, R. D. Tilley, *Nat. Catal.* **2022**, *5*, 231–237.
- [24] D. Chen, T. Gao, Z. Wei, M. Wang, Y. Ma, D. Xiao, C. Cao, C. Lee, P. Liu, D. Wang, S. Zhao, H. Wang, L. Han, *Adv. Mater.* **2024**, *36*, 2410537.

- [25] M. Kim, S. Kim, J. Park, S. Lee, I. Jang, S. Kim, C. Y. Lee, O. J. Kwon, H. C. Ham, J. T. Hupp, N. Jung, S. J. Yoo, D. Whang, *Adv. Funct. Mater.* **2023**, *33*, 2300673.
- [26] Y. Liu, L. Xing, Y. Liu, D. Lian, M. Chen, W. Zhang, K. Wu, H. Zhu, Z. Sun, W. Chen, P. Wu, D. Wang, Y. Ji, *Appl. Catal. B Environ. Energy* **2024**, *353*, 124088.
- [27] B. Zhang, Y. Chang, Y. Wu, Z. Fan, P. Zhai, C. Wang, J. Gao, L. Sun, J. Hou, *Adv. Energy Mater.* **2022**, *12*, 2200321.
- [28] T. Ma, P. Wang, H.-J. Niu, Z. Che, G. Li, W. Zhou, *Carbon* **2024**, *218*, 118758.
- [29] Z. Li, F. Meng, X. Yang, Y. Qi, Y. Qin, B. Zhang, *ACS Catal.* **2024**, *14*, 5016–5026.
- [30] G. Li, H. Jang, S. Liu, Z. Li, M. G. Kim, Q. Qin, X. Liu, J. Cho, *Nat. Commun.* **2022**, *13*, 1270.
- [31] C. Lyu, Y. Li, J. Cheng, Y. Yang, K. Wu, J. Wu, H. Wang, W. M. Lau, Z. Tian, N. Wang, J. Zheng, *Small* **2023**, *19*, 2302055.
- [32] C. Lyu, J. Cheng, H. Wang, Y. Yang, K. Wu, P. Song, W.-m. Lau, J. Zheng, X. Zhu, H. Y. Yang, *Adv. Compos. Hybrid Mater.* **2023**, *6*, 175.
- [33] Y. Zhu, J. Wang, T. Koketsu, M. Kroschel, J.-M. Chen, S.-Y. Hsu, G. Henkelman, Z. Hu, P. Strasser, J. Ma, *Nat. Commun.* **2022**, *13*, 7754.
- [34] X. Yue, D. Zheng, M. Gao, K. Wang, Z. Zhang, W. Dai, X. Fu, *ACS Catal.* **2023**, *13*, 15841–15850.
- [35] N. T. T. Thao, K. Kim, J. H. Ryu, B. S. An, A. K. Nayak, J. U. Jang, K. H. Na, W. Y. Choi, G. Ali, K. H. Chae, M. Akbar, K. Y. Chung, H. S. Cho, J. H. Park, B. H. Kim, H. Han, *Adv. Sci.* **2023**, *10*, 2207695.
- [36] A. Zhou, D. Wang, Y. Li, *Microstructures* **2022**, *2*, 2022005.
- [37] X. Zhao, Z. H. Levell, S. Yu, Y. Liu, *Chem. Rev.* **2022**, *122*, 10675–10709.
- [38] J. Liu, S. Wang, Y. Tian, H. Guo, X. Chen, W. Lei, Y. Yu, C. Wang, *Angew. Chem. Int. Ed.* **2024**, *64*, e202414314.
- [39] Z. Yang, J. Wang, C. Zhang, S. Wang, C. Xue, G. Tian, H. Su, C. Yan, Z. Yan, Y. Tian, *MGE Advances* **2024**, *2*, e22.
- [40] Y. Li, W. Wang, M. Cheng, Y. Feng, X. Han, Q. Qian, Y. Zhu, G. Zhang, *Adv. Mater.* **2023**, *35*, 2206351.

Manuscript received: February 18, 2025

Revised manuscript received: April 01, 2025

Accepted manuscript online: April 02, 2025

Version of record online: ■■■■■

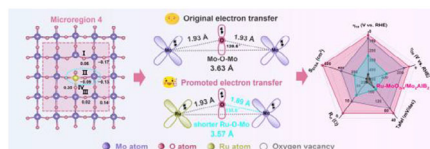
Research Article

Hydrogen Evolution

Y. Yang, D. Pang, C. Wang, Z. Fu, N. Liu,
J. Liu, H. Wu, B. Jia*, Z. Guo*, X. Fan*,
J. Zheng* ————— e202504084

Vacancy and Dopant Co-Constructed
Active Microregion in Ru–
MoO_{3-x}/Mo₂AlB₂ for Enhanced Acidic
Hydrogen Evolution

A novel Ru-doped low crystalline-crystalline MoO_{3-x}/Mo₂AlB₂ hybrid material was designed. The region containing Ru atom and/or O vacancy is innovatively defined as the active microregion. The Ru–O–Mo bonds



with shorter bond lengths provide satisfactory preconditions for the electronic structure modulation of O atoms. The ΔG_{H^*} of electron-rich O atoms is close to 0, which can effectively enhance the catalytic activity of HER.